Arzilli, F., La Spina, G., Burton, M., Polacci, M., Le Gall, N., Hartley, M., Di Genova, D., Cai, B., Vo, N., Bamber, E., Nonni, S., Atwood, R., Llewellin, E., Brooker, R., Mader, H., & Lee, P. (2019). Magma fragmentation in highly explosive basaltic eruptions induced by rapid crystallisation. *Nature Geoscience*, *12*, 1023–1028. https://doi.org/10.1038/s41561-019-0468-6

Accepted version before minor changes;

Magma fragmentation in highly explosive basaltic eruptions induced by rapid crystallisation

Fabio Arzilli[1], Giuseppe La Spina[1], Mike R. Burton[1], Margherita Polacci[1], Nolwenn Le Gall[2], Margaret E. Hartley[1], Danilo Di Genova[3], Biao Cai[4], Nghia T. Vo[5], Emily C. Bamber[1], Sara Nonni[5], Robert Atwood[5], Ed W. Llewellin[6], Richard A. Brooker[7], Heidy Mader[7] and Peter D. Lee[2]

[1]School of Earth and Environmental Sciences, University of Manchester, Manchester M139PL, UK

[2]Department of Mechanical Engineering, University College London, London, UK

[3]Institute of Non-Metallic Materials, Clausthal University of Technology, Zehntner Str. 2a, 38678 Clausthal-Zellerfeld, Germany

[4] School of Metallurgy and Materials, University of Birmingham, Birmingham B15 2TT, UK

[5]Diamond Light Source, Harwell Science and Innovation Campus, Didcot OX11 0DE, UK

[6]Department of Earth Sciences, Durham University, Durham DH1 3LE, UK

[7]School of Earth Sciences, University of Bristol, Bristol BS8 1RJ, UK

[*]Corresponding author: Dr. Fabio Arzilli

Corresponding author present affiliation: School of Earth and Environmental Sciences, The University of Manchester, Oxford Road, Manchester, M13 9PL, UK

E-mail address: fabio.arzilli@manchester.ac.uk

Phone: +393298429732; +447904104670

Basaltic eruptions are the most common form of volcanism on Earth and planetary bodies. The low viscosity of basaltic magmas inhibits fragmentation, favouring effusive and lava-fountaining activity, yet highly explosive, hazardous basaltic eruptions do occur. The processes that promote fragmentation of basaltic magma remain unclear, and are subject to debate. Here, we use a numerical conduit model to show that rapid ascent of magma during explosive eruption produces large undercooling. Novel *in situ* experiments reveal that undercooling drives exceptionally rapid (~minutes) crystallisation, inducing a step-change in viscosity that triggers magma fragmentation. Experimentally-produced textures are consistent with products of basaltic Plinian eruptions. We apply the numerical model to investigate basaltic magma fragmentation over a wide parameter space and find that all basaltic volcanoes have the potential to produce highly explosive eruptions. The critical requirements are initial magma temperatures lower than 1100 °C, in order to reach a syn-eruptive crystal content of > 30 vol.%, and thus a magma viscosity ≥ 10^5 Pa s, which our results suggest is the minimum viscosity required for the fragmentation of fast ascending basaltic magmas. Our study provides both a demonstration and explanation of the processes that drive basaltic Plinian eruptions, revealing how typically effusive basaltic volcanoes can produce unexpected highly explosive, and hazardous, eruptions.

Explosive eruptions are undoubtedly the most violent and catastrophic expression of volcanic activity[1,2]. Highly explosive Plinian eruptions can inject > 0.1 km^3 of pyroclastic material producing volcanic plumes that can reach up to 40 km in height, impacting both regional and global climate, and producing a significant threat to proximal populations[3,4]. Basaltic volcanoes are usually characterised by effusive and mild-explosive lava fountaining activity[5], however, basaltic Plinian eruptions can occur[6-11]. The main process characterising highly explosive activity is magma fragmentation, which is the transition from ductile to brittle behaviour of molten magma[1,2]. For silicic magmas, fragmentation is attributed to high strain rates associated with acceleration of the bubbly mixture[1,12-14] or from the bubble overpressure associated with restricted bubble expansion[14,15-18]. The low viscosity of basaltic magmas, however, makes high strain rates, or the bubble overpressure necessary to trigger fragmentation difficult to achieve[1,19].

Crystallisation during magma ascent may significantly increase magma viscosity, leading to fragmentation[20]. However, crystallisation in basaltic magmas has previously been thought to occur on timescales significantly longer than the time required for magma to ascend from a crustal storage chamber to the vent[21], particularly in the case of highly explosive eruptions.

In volcanic conduits, the crystallisation kinetics of an ascending magma are driven by degassing and cooling[22-23]. Plagioclase and pyroxene crystallisation are sensitive indicators of magma dynamics in volcanic conduits[21,24-27] and their kinetically controlled abundance can rapidly change magma rheology[28-29]. Our understanding of crystallisation kinetics in magmas is underpinned by *ex situ* crystallisation quench experiments. Here we perform novel *in situ* experiments in order to visualize and quantify the evolution of rapid crystallisation in basaltic magmas, as with this approach it is possible to ascertain in real time when crystals start to form and how quickly magma crystallinity evolves.

A frequently used model to describe crystallisation as function of time is given by an exponential law[21,23], where the rate of crystallisation is controlled by the characteristic time $\tau^{(c)}$. The characteristic time is a measure of how fast a process will approach the equilibrium[21,30]. The smaller

$\tau^{(c)}$, the faster crystals reach their equilibrium abundance (see Methods section). La Spina et al. (ref. 21) demonstrated that the time required to reach the equilibrium crystal fraction in basalts is ~4.6 times $\tau^{(c)}$. Furthermore, during mild lava-fountaining basaltic activity[21], $\tau^{(c)}$ is in the order of thousands seconds, resulting in a crystallisation time of ~2 hours. Crystallisation rate increases with magma ascent rate, as cooling and decompression rates increase[30-34]. Therefore, $\tau^{(c)}$ is smaller and the equilibrium crystal fraction will be reached faster. However, the characteristic times of crystal growth during fast magma ascent have not been quantified.

In order to quantify the characteristic times of plagioclase and pyroxene crystallisation during rapid ascent of basaltic magma, here we present the first *in situ* 4D (3D plus time) crystallisation kinetics experiments under fast cooling rates, using fast synchrotron X-ray microtomography. Our experiments provide the first estimation of the characteristic time for plagioclase and pyroxene crystallisation in trachybasaltic magmas during a rapid and continuous increase of undercooling, where ΔT is defined as the difference between the highest temperature at which plagioclase and pyroxene is expected to crystallise and the temperature of the magma[24-27].

Crystallisation experiments at high undercooling

Crystallisation experiments were performed *in situ* at beamline I12-JEEP, Diamond Light Source, Harwell, UK, using a trachybasaltic glass (Supplementary Table 1) from the 2001 Etna eruption as the starting material (see Methods). We combined a bespoke high-temperature environmental cell[35] with fast synchrotron X-ray microtomography to image the evolution of crystallisation in real time[36] in two experiments. In the first part of the experiment, crystallisation was induced by decreasing temperature from 1250 °C to either 1170 °C or 1150 °C at 0.4 °C s^{-1} at ambient pressure with a dwell time at the final temperature of 4 h[36] (Supplementary Fig. 1). During these 4 h, blocky and prismatic clinopyroxene and oxide crystals were able to grow[36] (Fig. 1 and Supplementary Figs. 2 and 3), and the residual melt evolved to a basaltic trachyandesitic composition (Supplementary Table 1; Supplementary Figs. 2 and 3). After 4 h at sub-liquidus

conditions (1170 °C and 1150 °C), the system was perturbed through a rapid cooling rate of 0.4 °C s^{-1}, inducing a sudden and continuous increase of undercooling (ΔT). This produced a rapid crystallisation event from the residual melt (Fig. 1; Supplementary Figs. 2 and 3). Our results show that skeletal plagioclase crystals grew during this final stage of rapid cooling, specifically between 1112 and 1073 °C after a dwell time of 4 hours at 1150 °C (Fig. 1) and between 1131 and 1053 °C after a dwell time of 4 hours at 1170 °C (Supplementary Fig. 3a,b,c). Plagioclase crystals grew to equilibrium abundance in ~100 seconds (Fig.1), i.e. between two 3D scans. Following this initial burst of rapid plagioclase growth, dendritic clinopyroxene crystals began to nucleate heterogeneously on plagioclase and grew to their final size in the following 180 seconds (Fig. 1b,c; Supplementary Figs. 2b,c, 3d,e, 4 and 5).

The large ΔT reached in a relatively short time during our *in situ* 4D crystallisation experiments generated distinctive skeletal plagioclase crystals with swallow-tail morphology and dendritic pyroxene (Fig. 2a-c), similar to the skeletal plagioclase and dendritic pyroxene crystals observed in the products of explosive basaltic Plinian eruptions[7-11,37,38], such as Etna 122 B.C.[7,8,37,38] (Fig. 2d). Heterogeneous nucleation of dendritic pyroxene on skeletal plagioclase (Fig. 1b) is observed to occur in ~180 s during our 4D experiments. These distinctive textures are also reported in products of the Fontana Lapilli (Nicaragua)[11,37,38] and 1886 Tarawera (New Zealand) eruptions[7,9,10]. Therefore, all the studied examples of basaltic Plinian deposits show features that are consistent with the textures produced in our experiments. Furthermore, the signature skeletal and dendritic pyroxene is also observed in sub-Plinian eruption (Yufune 2) products of Mt. Fuji (Japan)[39].

Skeletal plagioclase crystallisation occurred at ΔT between 60 and 140 °C with a growth rate of $3x10^{-5}$ cm s^{-1} (mm h^{-1}) (Supplementary Table 2), whilst dendritic pyroxene crystallised at ΔT between 60 and 175 °C with a growth rate of $2x10^{-5}$ cm s^{-1} (mm h^{-1}) (Supplementary Table 2). This indicates that a rapid increase of ΔT (>60 °C) induces fast crystallisation. As the equilibrium pyroxene crystal content is achieved within ~180 s, we can infer that the pyroxene characteristic time under large ΔT is < 40 s. For plagioclase, where the equilibrium crystal content is achieved

within 90 s the characteristic time is < 20 s. These are about two orders of magnitude less than the characteristic time found by La Spina et al. (ref. 21) for effusive and mild lava fountaining activity at Etna (Italy), Stromboli (Italy) and Kilauea (Hawaii), which involved much smaller ΔT (30-60 °C)[21] and magma ascent rates of ~3 m s^{-1}.

Ex situ experiments were also performed using a TZM cold seal pressure vessel apparatus, in order to investigate whether fast crystallisation also occurs in a hydrous trachybasaltic melt during rapid and continuous cooling and decompression (see Methods), simulating fast magma ascent in the conduit. The experimental approach consisted of holding the sample for 30 minutes at 75 MPa and 1070 °C before the sample was decompressed and the temperature decreased. After 30 minutes pressure and temperature were decreased continuously for 300 s at 0.2 MPa s^{-1} and 0.2 °Cs^{-1} respectively, reaching 15 MPa and 1010 °C (Supplementary Table 3; Supplementary Fig. 6). The rapid decompression and cooling enabled large ΔTs to be the achieved (>100 °C; see Supplementary Fig. 6) in 300 s, favouring predominantly clinopyroxene crystallisation, with minor plagioclase and oxide (Supplementary Fig. 7). This indicates that $\tau^{(c)}$ is < 60 s, in agreement with the order of magnitude estimated from *in situ* experiments.

Large undercooling can produce significant syn-eruptive microlite crystallisation during rapid magma ascent[24-27]. This increase in crystallinity dramatically increases the viscosity of the magma[19]. This process has been proposed to explain explosive basaltic Plinian eruptions, supported by evidence of high microlite contents[7-11,37,38]. However, a mechanism for this exceptionally fast crystallisation during rapid magma ascent in basaltic Plinian eruptions, favouring fragmentation, has not been demonstrated so far.

Numerical simulation of the 122 B.C. Etna basaltic Plinian eruption

Magma fragmentation in basaltic Plinian eruptions has been investigated with conduit models, where crystallisation has been assumed either to be constant[20] or at equilibrium[40]. Recent results demonstrate that disequilibrium crystallisation plays a fundamental role in magma dynamics within

147 the conduit[21], but syn-eruptive disequilibrium crystallisation has not yet been considered for basaltic
148 explosive volcanism[20,40].

149 We used the conduit model described by La Spina et al. (ref. 21, 23) to investigate the effect of
150 the new experimentally constrained characteristic times for crystallisation with large undercooling
151 derived here on the ductile-brittle transition of basaltic magma during highly explosive eruptions.
152 Since we are focussing our attention on explosive eruptions with high mass eruption rates (>10^6
153 kg/s), it is reasonable to assume that outgassing is negligible for this kind of activity. Indeed,
154 outgassing will be inhibited by fast magma ascent and fragmentation will be achieved faster than
155 outgassing[41]. As a test case, we consider the 122 B.C. Etna basaltic Plinian eruption[6-8]. To model
156 fragmentation we adopt the strain-rate criterion introduced by Papale (ref. 1):

157 $$\dot{\gamma} = k\frac{G_\infty}{\mu} \quad (1)$$

158 where $\dot{\gamma}$ is the elongational strain rate, k=0.01 is a constant, μ is the magmatic viscosity and G_∞
159 is the elastic modulus at infinite frequency. The other constitutive equations are reported in the
160 Methods section. In Figure 3 we report the calculated plagioclase undercooling, crystal content and
161 viscosity as function of depth for $\tau^{(c)}$ = 10 and 1000 s. Large undercooling is produced by adiabatic
162 expansion of exsolved volatiles, and mitigated by the latent heat of crystallisation for $\tau^{(c)}$ = 10 s
163 (Fig. 3a). In this case, numerical results show a rapid increase in crystallinity and in viscosity at
164 depths below 2 km (Fig. 3c), leading to fragmentation and explosive Plinian eruption. Importantly,
165 numerical results indicate that strain-induced fragmentation is favoured by a combination of rapid
166 viscosity increase (about one order of magnitude in 5 seconds approaching the fragmentation depth)
167 and fast decompression/ascent rates (~0.2 MPa s^{-1} and ~15 m s^{-1}) that generate high strain rates. For
168 $\tau^{(c)}$ = 1000 s, instead, the crystallisation rate is slow, and viscosity stays within the fragmentation
169 threshold all along the conduit.

170

171 **Sensitivity analyses on basaltic magma fragmentation driven by rapid crystallisation**

Having established that fast crystallisation plays an important role on basaltic Plinian eruptions, we performed a sensitivity study with our numerical model to investigate the parameter space whereby basaltic fragmentation driven by rapid crystallisation may occur. We use the Etna 122 B.C. eruption as a test case. We focus on the behaviour of ΔT as a function of characteristic time of crystallisation, pressure, temperature and magmatic H_2O content at the conduit inlet, conduit radius, and initial phenocryst content. A detailed description of the initial condition of the sensitivity study can be found in the Methods section. We performed several sensitivity studies assuming a characteristic time of $\tau^{(c)}$ = 10 s, as observed in our experiments, and $\tau^{(c)}$ = 1000 s, as observed for Etna 2001 in mild explosive activity. We also examined $\tau^{(c)}$ = 1 and 100 s for completeness.

Numerical results show that undercooling is principally controlled by $\tau^{(c)}$ (Fig. 4a), because the release of latent heat during rapid crystallisation (i.e. small $\tau^{(c)}$) affects the temperature of the system, and, consequently, the undercooling. Therefore, undercooling and characteristic time are linked, affecting one each other. However, our numerical results indicate that, within the parameters space investigated, ΔT is always maintained between 60 and 190 °C (Fig. 4b), which is enough to enable rapid crystallisation in any case. Furthermore, the sensitivity analyses indicate that, after the characteristic time, initial temperature and water content (exsolved + dissolved) play an important role on controlling undercooling (Fig. 4a). ΔT at the point of fragmentation increases as initial temperature decreases (Fig. 4b), meaning that cooler magma in the chamber is more likely to produce microlite crystallisation during ascent, as ΔT will already be large under the pre-eruptive condition. An increase in the initial total H_2O (exsolved + dissolved) also produces an increase of ΔT (Fig. 4c), caused by greater cooling of the system due to enhanced adiabatic gas expansion. Furthermore, higher water content favours rapid crystallisation of microlites, due to the increase in diffusivity within the melt.

Our sensitivity studies show that a lower initial temperature and a higher pre-eruptive crystal content results in a greater likelihood of explosive eruptions (Fig. 4d,e). This is consistent with estimates of pre-eruptive temperatures obtained for the Etna and Fontana Plinian eruptions, which

198 range between 1000 and 1060 °C[37]. Regarding the pre-eruptive crystal content, however, products
199 erupted from basaltic Plinian eruptions are characterized by a small phenocryst content (<10
200 vol.%)[7,8,10,11,37,38,40]. Therefore, in this context of low initial temperature and low phenocryst
201 content, our results highlight that the characteristic time of crystallisation has a fundamental role on
202 the likelihood of producing an explosive eruption. Indeed, a small $\tau^{(c)}$ is the primary cause for a
203 significant increase of the syn-eruptive crystal fraction over short timescales during magma ascent,
204 which consequently increases magma viscosity and, thus, the probability of magma fragmentation
205 (Fig. 4f). Moreover, our sensitivity analysis demonstrates that when the syn-eruptive crystal content
206 exceeds 30 vol.%, all numerical solutions reach the fragmentation threshold (Fig. 4f). Indeed, in a
207 fast ascending magma (from our sensitivity analyses we have an average ascent rate between ~5-50
208 m/s), this increase in syn-eruptive crystal content produces a rapid and dramatic increase of
209 viscosity (about one order of magnitude in less than 10 s close to the fragmentation depth),
210 increasing the likelihood of magma fragmentation. Numerical results also show that, as soon as
211 viscosity exceeds 10^5 Pa s, all the numerical solutions reach the fragmentation threshold, generating
212 an explosive eruption (Fig 4g). Indeed, for a fast ascending magma where outgassing can be
213 neglected and strain-rates are high, the key parameter controlling the triggering of fragmentation is
214 viscosity. Therefore, 10^5 Pa s represents a minimum viscosity determining a drastic change in
215 eruptive style for activities characterised by high mass eruption rates. This minimum viscosity is
216 one order of magnitude lower than previously reported for low-viscosity magmas[1,42].

217 Experimental and natural observations combined with a numerical model allow us to conclude
218 that pre-eruptive temperatures <1100 °C favour the formation of highly explosive basaltic
219 eruptions, such as Plinian volcanism, driven by fast syn-eruptive crystal growth under high
220 undercooling. This implies that all basaltic systems on Earth have the potential to produce powerful
221 explosive eruptions.

METHODS

Starting material. The starting material, used for our crystallisation experiments, is a trachybasalt from the lower vents of the 2001 Mt. Etna eruption[36,43]. The anhydrous, glassy starting material was obtained by melting crushed rock samples in a Pt crucible. Melting was performed in a Nabertherm® $MoSi_2$ box furnace at 1400 °C and at atmospheric pressure. The melt was left in the furnace for four hours to allow the melt to fully degas and to dissolve the crystals present. The melt was then quenched in air to glass. This procedure was repeated two times to homogenise the melt. Finally, anhydrous glassy cylinders 3 mm in diameter and 4 mm in length were drilled from the synthesized glass for *ex situ* and *in situ* 4D crystallisation experiments.

The chemical composition of the anhydrous glassy starting material has been analysed with a Jeol JXA 8530 F microprobe at the Photon Science Institute, University of Manchester, Manchester, UK, and are reported in Supplementary Table 1. Analyses were performed using a 15 kV accelerating voltage, 10 nA beam current and beam size of 10 μm. Standards used for calibration were albite for Na, periclase for Mg, corundum for Al, fayalite for Fe, tephroite for Mn, apatite for P, sanidine for K, wollastonite for Ca and Si and rutile for Ti. Sodium and potassium were measured first to minimize loss owing to volatilisation.

Hydrous trachybasaltic glass with ~3 wt. % of H_2O was obtained melting the starting material and homogenizing H_2O in a Pt capsule at 100 MPa and 1200 °C. The hydrous starting glasses were produced using a TZM cold seal pressure vessel apparatus at the School of Earth Sciences, University of Bristol, Bristol, UK. Before to perform crystallisation experiments Raman spectra were collected from the hydrous starting glass, using a Thermo ScientificTM DXRTMxi Raman Imaging Microscope at the School of Earth Sciences, University of Bristol (Bristol, UK) in order to check that the amount of H_2O was ~3 wt. %.

***Ex situ* decompression and cooling experiments.**

Ex situ experiments were performed in order to investigate the process of fast crystallisation in a hydrous trachybasaltic melt during a continuous decompression (0.2 MPa s^{-1}) and cooling (0.2 °Cs^{-1}), simulating magma ascent in the conduit. Two experiments were performed using a TZM cold seal pressure vessel apparatus at the School of Earth Sciences, University of Bristol, Bristol, UK. The redox condition of the apparatus was NNO, adding ~1 vol.% of hydrogen to the pressuring argon. Capsules (Au_{80}-Pd_{20}) were loaded with hydrous glass with a cylindrical shape. The experimental approach consisted of holding the sample for 30 minutes at 75 MPa and 1070 °C before being decompressed and cooled. The first experiment was quenched after 30 minutes at 75 MPa and 1070 °C, in order to texturally characterise the initial conditions before that fast decompression and cooling were applied. In the second experiment, after 30 minutes pressure and temperature were released continuously in 300 s at 0.2 MPa s^{-1} and 0.2 °Cs^{-1} respectively, reaching 15 MPa and 1010 °C (Supplementary Table 3; Supplementary Fig. 6). The sample was rapidly quenched at the final conditions. Final pressure was chosen as approximate fragmentation pressures calculated by modeling. Decompression and cooling rates were predicted from the conduit model for magma ascent during basaltic Plinian eruptions.

***In situ* synchrotron X-ray microtomography experiments.** The experiments were performed at the beamline I12-JEEP[44], Diamond Light Source, Harwell, UK. For these *in situ* crystallisation experiments, we used the high-temperature resistance Alice furnace[45], which allows us to control cooling at 0.05 °Cs^{-1} to 0.4 °Cs^{-1}, and the P2R in situ rig[35] for high speed rotation. Temperature was measured with a R type thermocouple, which was close to the sample, positioned in the middle of the hot spot. The dimension of the Alice furnace's hot spot with homogeneous temperature is ~5x5x5 mm; our samples were positioned within this area. The R type thermocouple provided us the temperature of the sample with an uncertainty of ±5 °C. The sample holder was an alumina crucible (Supplementary Fig. 2), which is suitable for the temperature range investigated and it has low X-ray attenuation coefficient. The glassy cylinders were heated *in situ* in the Alice furnace up

to 1250 °C for 30 minutes (Supplementary Figure 1). After the initial annealing period, crystallisation was induced by decreasing temperature from 1250 °C to 1170 °C or 1150 °C at ambient pressure, holding at the final temperature for 4 h[36] (Supplementary Figure 1). After this step, the system was perturbed by a rapid cooling at rate of 0.4 °Cs^{-1} in order to investigate the rapid crystallisation in real time (Supplementary Figure 1), reaching high undercooling (up to ~180 °C) in a short time.

The experiments were performed in phase-contrast mode, setting the sample-to-detector distance at 2300 mm in order to work in the edge-detection regime[46] (Supplementary Table 4). The projections were acquired using a monochromatic X-ray beam with energy of 53 keV. In each scan, 1800 tomographic projections were acquired by the detector with equiangular steps over a full rotation angle of 180° (Supplementary Table 4). The exposure time for the acquisition of each projection was 0.05 s (Supplementary Table 4), therefore, the temporal resolution of each scan was of 90 seconds. The isotropic pixel size is 3.2 μm. The detector was a high-resolution imaging PCO edge camera with optical module 3, corresponding to a field of view of 8.0 mm × 7.0 mm. Scan acquisition started before the end of the annealing, covering the cooling period between 1250 °C and the dwell temperatures (1170 and 1150 °C), the entire duration of the dwell time and the final rapid cooling rate of 0.4 °Cs^{-1}.

Image reconstruction and processing. Tomographic projections were reconstructed into 32-bit slices by using Diamond I12 in-house python codes, using the *gridrec* algorithm[47,48] (http://confluence.diamond.ac.uk/display/I12Tech/Reconstruction+scripts+for+time+series+tomography)[49,50]. The pre-processing pipeline includes centre of rotation calculation[49], zinger removal, blob removal[50], and regularisation-based ring removal[51].

The reconstructed slices were converted to 8-bit raw format and stacked using ImageJ software[52] to obtain volumes in which the isotropic voxel has an edge size of 3.2 μm. Reconstructed volumes of experiments ET1150 and ET1170 were then cropped using Avizo® software v.8.0 (FEI

299 Visualization Sciences Group) in order to select the volume of interest (VOI) (Supplementary Table
300 4). In the experiment ET1150 plagioclase and pyroxene crystals nucleated and grew in a relatively
301 large pocket of melt (Figs 1 and 2). Therefore, the VOI selected consists of a volume of melt where
302 the rapid crystallisation of plagioclase and pyroxene occurred during the final rapid cooling rate of
303 0.4 °Cs^{-1}. In the experiment ET1170 plagioclase and pyroxene crystals formed in narrow layers of
304 melt (Supplementary Fig. 3), during rapid continuous cooling at a rate of 0.4 °Cs^{-1}.
305 Three-dimensional visualization (volume rendering) of the reconstructed volumes was obtained
306 using the commercial software VGStudio 3.0 (Volume Graphics), which allowed us to make 3D
307 textural observations of the plagioclase and pyroxene crystal morphologies (Fig. 2). Therefore, the
308 reconstructed volume of each scan allowed us to quantify when and at which range of temperature
309 plagioclase and pyroxene crystals were able to form.
310
311 **Image segmentation and analysis of plagioclase**. Segmentation is the process that allows
312 separation of objects from the background to obtain binary volumes containing only the feature of
313 interest. Segmentation of plagioclase crystals from the glassy matrix was performed using the semi-
314 automatic volume segmentation[53,54] in Avizo software v. 8.0 (Supplementary Table 4). This
315 segmentation requires manual drawing of the outlines of crystals on the 2D slices. This is repeated
316 every 5–10 slices, depending on the size of the crystal and the complexity of their shape, along the
317 crystal length. The crystal shape is reconstructed automatically by the software through an
318 interpolation procedure. The advantage of this technique is that the operator can obtain the real
319 morphology of the object of interest by visual inspection[53,54].
320 The reconstructed 3D images were processed and analysed with the Pore3D software library,
321 custom-developed at Elettra[55]. The Pore3D software allowed us to quantify the number of
322 plagioclase crystals, the volume and the maximum length of each crystal, operating directly in the
323 3D domain[55,56]. As we were able to obtain the 3D shape of plagioclase crystals and the real
324 maximum axis length (L_{3D}) we could calculate the growth rate (Y_{L3D}) of plagioclase crystals

(Supplementary Table 2), using the experimental duration of growth (experimental duration). The growth rate was estimated using the following equation[53]:

$$Y_{L3D} = (L_{3D}*0.5)/t_{growth}$$

where t_{growth} is the time required for crystal growth. The microtomography images give us the opportunity to measure the volume of crystals. The volumetric growth rate (Y_V) was calculated (Supplementary Table 2) using the following relationship[53]:

$$Y_V = (V*0.5)/t_{exp}$$

where V is the volume of the crystal.

Image analysis of pyroxene growth kinetics. Back-scattered electron (BSE) images were collected, using a JEOL JSM-6390LA FE-SEM at the School of Earth and Environmental Sciences, University of Manchester, Manchester, UK, in order to analyse the pyroxene morphologies and kinetics. We used an acceleration voltage of 15 kV and beam current of 10 nA. The sizes of dendritic pyroxene crystals were measured in the 2D domain, using BSE images and ImageJ software[52], as pyroxene morphologies formed during continuous cooling are difficult to resolve and analyse in the 3D domain. The pyroxene growth rate is calculated by dividing the entire length of the dendritic crystal over the duration of the pyroxene growth (Supplementary Table 2), as dendritic crystals grow in one direction.

Electron microprobe analysis. Samples obtained with *ex situ* and *in situ* crystallisation experiments were analysed with a JEOL JXA-8530F field emission electron microprobe at the Photon Science Institute, University of Manchester, Manchester, UK. For both instruments, the operating conditions were as follows: 15 kV accelerating voltage, 10 nA beam current, and beam diameter of 10 or 5 μm (the latter for microlites). Sodium and potassium were measured first to minimise loss by volatilisation. Calibration standards were albite for Na, periclase for Mg, corundum for Al, fayalite for Fe, tephroite for Mn, apatite for P, sanidine for K, wollastonite for Ca

and Si and rutile for Ti. Several compositional maps, with a nominal resolution of 1 μm2, have been also collected using the EPMA (EPMA map, are reported in Supplementary Figs. 4, 5 and 7).

Constitutive equations for the conduit model. In this work we use the 1D steady-state model for magma ascent described by ref. (21, 23, 57). The governing equations used in this work are reported in ref. (57). The application to a specific volcano is achieved by providing constitutive equations to describe the specific rheological, solubility, crystallisation, outgassing, and fragmentation behaviour of the system.

Following ref. (58), the viscosity of the liquid phase is modelled as:

$$\mu_l = \mu_{melt} \cdot \theta(x_c^l),$$

where μ_{melt} is the viscosity of the bubble-free, crystal-free liquid phase and θ is a factor which increases viscosity attributed to the presence of crystals[59].

We use an empirical relationship to estimate μ_{melt} as a function of water concentration and temperature, as in ref. (60) (based on the Vogel-Fulcher-Tammann equation):

$$\log(\mu_{melt}) = \mathrm{A} + \frac{\mathrm{B}(\mathrm{y}, x_{d_{H_2O}}^{md})}{T - \mathrm{C}(\mathrm{y}, x_{d_{H_2O}}^{md})},$$

where the viscosity μ_{melt} is in Pa s and *T* is the temperature in Kelvin. The parameter A is the logarithmic value of the viscosity at infinite temperature and it is assumed to be constant for all melts. The parameters B and C, instead, are functions of the melt composition *y* and of the dissolved water content $x_{d_{H_2O}}^{md}$. In this work, we used the composition of the average melt inclusion composition (Etna 122 B.C.) from ref. (61). Furthermore, as crystallisation proceeds, viscosity is increased according to the empirical model described in ref. (62):

$$\theta = \frac{1 + \varphi^{\delta}}{[1 - F(\varphi, \xi, \gamma)]^{B\phi^*}},$$

where

374 $$F = (1-\xi)erf\left[\frac{\sqrt{\pi}}{2(1-\xi)}\varphi(1+\varphi^{\gamma})\right], \quad \varphi = \frac{\left(\sum_{j=1}^{n_c} x_{c_j}^{l}\right)}{\phi^{*}}.$$

375 The fitting parameters B, δ, ξ, γ and ϕ^{*} chosen for this work are the same used in ref. (63).

376 The model proposed in this work takes into account two different gas components: water and
377 carbon dioxide. The equilibrium profile of the dissolved gas content $x_{d_i}^{md,eq}$ of component i follows
378 the Henry's Law, i.e.

379 $$x_{d_i}^{md,eq} = \sigma_i \left(\frac{P_{g,i}}{\bar{P}}\right)^{\varepsilon_i},$$

380 where $P_{g,i} = \alpha_{g_i} P_g / \alpha_g$ is the partial pressure of the i-th gas component expressed in Pa, $\bar{P} = 1$
381 Pa is used to make the expression in the brackets adimensional, σ_i is the solubility coefficient and ε_i
382 is the solubility exponent. We assume that the solubility parameter σ_i and ε_i are constant during
383 ascent. For this work we adopted the following parameters $\sigma_{H_2O} = 1.8911 \times 10^{-6}$; $\varepsilon_{H_2O} = 0.5257$;
384 $\sigma_{CO_2} = 2.2154 \times 10^{-12}$; $\varepsilon_{CO_2} = 1.075$. In this work, we assume also equilibrium exsolution, which
385 means that the dissolved volatile contents always follow the equilibrium profile.

386 The crystallisation model adopted here has been proposed in ref. (23). We consider the three
387 different major crystal components erupted by Etna volcano: plagioclase, pyroxene and olivine. We
388 assume that crystals stay coupled with the melt (i.e. no fractional crystallisation). For a better
389 modelling of crystal nucleation and growth, we also assume that the equilibrium crystal contents are
390 functions of temperature, pressure and dissolved water content. With these assumptions, the
391 equilibrium mass fraction $x_{c_j}^{l,eq}$ of crystal phase j is computed using the polynomial function

392 $$x_{c_j}^{l,eq}(P^{*}, T^{*}, x_d^{*}) = \zeta_{j,1}(P^{*})^2 + \zeta_{j,2}(T^{*})^2 + \zeta_{j,3}(x_d^{*})^2 + \zeta_{j,4}(P^{*})(T^{*}) +$$
$$+\zeta_{j,5}(T^{*})(x_d^{*}) + \zeta_{j,6}(x_d^{*})(P^{*}) + \zeta_{j,7}(P^{*}) + \zeta_{j,8}(T^{*}) + \zeta_{j,9}(x_d^{*}) + \zeta_{j,10},$$

393 where P^{*} is the liquid pressure expressed in bars, T^{*} is the temperature expressed in Celsius
394 degrees and x_d^{*} is the dissolved water concentration in weight percent. From $x_{c_j}^{l,eq}$, the equilibrium
395 crystal volume fraction β_j^{eq} can be computed using the relation

$$\beta_j^{eq} = \frac{\rho_l x_{c_j}^{l,eq}}{\rho_{c_j}}.$$

The parameters $\zeta_{j,i}$ are calculated fitting the polynomial function over a large range of data obtained at different pressures, temperatures and water contents with alphaMELTS[64], a command line version of MELTS[65]. As previously, we used the average melt inclusion composition (Etna 122 B.C.) from ref. (61).

Disequilibrium crystallisation is considered in our model and characteristic times controls the time needed to reach equilibrium crystal content. The differential equation in the conduit model which describes the crystal volume fraction within the conduit is the following[21]:

$$\frac{\partial \alpha_l \rho_c \beta u_l}{\partial z} = -\frac{1}{\tau^{(c)}} \alpha_l \rho_c (\beta - \beta^{eq}).$$

Here, α_l is the volume fraction of the liquid phase, ρ_c is the density of the crystals, u_l is the velocity of the liquid phase, z is the vertical axis, β is the actual total crystal volume fraction, whereas β^{eq} is the equilibrium total crystal volume fraction. If we multiply all the terms by the characteristic time $\tau^{(c)}$, we notice that the smaller is $\tau^{(c)}$, the smaller has to be $(\beta - \beta^{eq})$. In other terms, the smaller is the characteristic time, the faster the crystals will reach the equilibrium value.

Formally, as described in La Spina et al. (ref. 21), the characteristic time reflects the time required to reduce the difference between the actual and the equilibrium value to e^{-1} (~37%) of the initial difference. This means that, if β_0 is the initial value of a physical parameter β (which, in our case, is the crystal volume fraction), and β_{eq} is the equilibrium value in response to a perturbation of the system, at the characteristic time τ, we have

$$\beta(\tau) = \beta^{eq} + e^{-1}(\beta_0 - \beta^{eq}).$$

The experimental phase diagram for Etna basalt erupted during the 122 B.C. eruption[37] provides the plagioclase and pyroxene liquidus at different pressures and temperatures, whilst the conduit model is able to track temperature evolution within the conduit. Combining both of these data, we can estimate ΔT with respect to the plagioclase and pyroxene liquidus during magma ascent.

For this work, as we are interested in the highly explosive activity, we assumed no relative velocity between gas and melt. Furthermore, as we indicated in the main text, we used as fragmentation model the strain-rate criterion introduced by ref. (1).

Initial condition for the sensitivity analysis.

The range of input parameters adopted for the sensitivity analysis are the following: 140–160 MPa for the inlet pressure at 6000 m depth, 1050–1100 °C for the magma inlet temperature, 5–30 m for the radius of the conduit, 2.0–4.0 wt.% for the total water content, 0.1–2.0 wt.% for the total CO_2 content, 0–20 vol.% for the initial phenocrysts, and 1–1000 s for the characteristic time of crystallisation. As we do not know the probability distribution of the uncertain input parameters, we have assumed a uniform distribution within the aforementioned ranges. The sensitivity analysis was performed on using the DAKOTA toolkit (Design Analysis Kit for Optimization and Terascale Applications)[66], an open-source software developed at Sandia National Laboratories that provides a flexible and extensible interface between analysis codes and iterative systems analysis methods such as uncertainty quantification, sensitivity analysis, optimization, and parameter estimation.

435 **References**

436 1. Papale, P. Strain-induced magma fragmentation in explosive eruptions. *Nature* **397**, 425
437 (1999).

438 2. Dingwell, D. B. (1996). Volcanic Dilemma--Flow or Blow?. Science, 273(5278), 1054-1055.

439 3. Carey, S., & Sigurdsson, H. (1989). The intensity of plinian eruptions. Bulletin of
440 Volcanology, 51(1), 28-40.

441 4. Wilson, L. (1976). Explosive volcanic eruptions—III. Plinian eruption columns. Geophysical
442 Journal International, 45(3), 543-556.

443 5. Polacci, M., Corsaro, R. A. & Andronico, D. Coupled textural and compositional
444 characterization of basaltic scoria: Insights into the transition from Strombolian to fire fountain
445 activity at Mount Etna, Italy. *Geology* **34**, 201-204 (2006).

446 6. Coltelli, M., Del Carlo, P. & Vezzoli, L. Discovery of a Plinian basaltic eruption of Roman
447 age at Etna volcano, Italy. *Geology* **26**, 1095-1098 (1998).

448 7. Houghton, B. F., Wilson, C. J. N., Del Carlo, P., Coltelli, M., Sable, J. E. & Carey, R. The
449 influence of conduit processes on changes in style of basaltic Plinian eruptions: Tarawera 1886 and
450 Etna 122 BC. *Journal of Volcanology and Geothermal Research* **137**, 1-14 (2004).

451 8. Sable, J. E., Houghton, B. F., Del Carlo, P. & Coltelli, M. Changing conditions of magma
452 ascent and fragmentation during the Etna 122 BC basaltic Plinian eruption: Evidence from clast
453 microtextures. *Journal of Volcanology and Geothermal Research* **158**, 333-354 (2006).

454 9. Houghton, B. F. & Gonnermann, H. M. Basaltic explosive volcanism: constraints from
455 deposits and models. *Chemie der Erde-Geochemistry* **68**, 117-140 (2008).

456 10. Sable, J. E. Houghton, B. F., Wilson, C. J. N. & Carey, R. J. Eruption mechanisms during the
457 climax of the Tarawera 1886 basaltic Plinian eruption inferred from microtextural characteristics of
458 the deposits. *Studies in Volcanology: The Legacy of George Walker. Special Publications of*
459 *IAVCEI* **2**, 129-154 (2009).

460 11. Costantini, L., Houghton, B. F. & Bonadonna, C. Constraints on eruption dynamics of
461 basaltic explosive activity derived from chemical and microtextural study: the example of the
462 Fontana Lapilli Plinian eruption, Nicaragua. *Journal of Volcanology and Geothermal Research* **189**,
463 207-224 (2010).
464 12. Melnik, O., & Sparks, R. S. J. (1999). Nonlinear dynamics of lava dome extrusion. Nature,
465 402(6757), 37.
466 13. Gonnermann, H. M., & Manga, M. (2003). Explosive volcanism may not be an inevitable
467 consequence of magma fragmentation. Nature, 426(6965), 432.
468 14. Gonnermann, H. M. (2015). Magma fragmentation. Annual Review of Earth and Planetary
469 Sciences, 43, 431-458.
470 15. Alidibirov, M., & Dingwell, D. B. (1996). Magma fragmentation by rapid decompression.
471 Nature, 380(6570), 146.
472 16. Zhang, Y. (1999). A criterion for the fragmentation of bubbly magma based on brittle failure
473 theory. Nature, 402(6762), 648.
474 17. Spieler, O., Kennedy, B., Kueppers, U., Dingwell, D. B., Scheu, B., & Taddeucci, J. (2004).
475 The fragmentation threshold of pyroclastic rocks. Earth and Planetary Science Letters, 226(1-2),
476 139-148.
477 18. Kueppers, U., Scheu, B., Spieler, O., & Dingwell, D. B. (2006). Fragmentation efficiency of
478 explosive volcanic eruptions: A study of experimentally generated pyroclasts. Journal of
479 Volcanology and Geothermal Research, 153(1-2), 125-135.
480 19. Giordano, D. & Dingwell, D. Viscosity of hydrous Etna basalt: implications for Plinian-style
481 basaltic eruptions. *Bulletin of Volcanology* **65**, 8-14 (2003).
482 20. Moitra, P., Gonnermann, H. M., Houghton, B. F. & Tiwary, C. S. Fragmentation and Plinian
483 eruption of crystallizing basaltic magma. *Earth and Planetary Science Letters* **500**, 97-104 (2018).

21. La Spina, G., Burton, M., Vitturi, M. D. M. & Arzilli, F. Role of syn-eruptive plagioclase disequilibrium crystallisation in basaltic magma ascent dynamics. *Nature communications* **7**, 13402 (2016).

22. Cashman, K. & Blundy, J. Degassing and crystallisation of ascending andesite and dacite. *Philosophical Transactions of the Royal Society of London A: Mathematical, Physical and Engineering Sciences* **358**, 1487-1513 (2000).

23. La Spina, G., Burton, M., de' Michieli Vitturi, M. Temperature evolution during magma ascent in basaltic effusive eruptions: a numerical application to Stromboli volcano. *Earth Planet. Sci. Lett.* **426**, 89–100 (2015).

24. Hammer, J. E. & Rutherford, M. J. An experimental study of the kinetics of decompression-induced crystallization in silicic melt. *Journal of Geophysical Research: Solid Earth* **107**, ECV-8 (2002).

25. Couch, S., Harford, C. L., Sparks, R. S. J. & Carroll, M. R. Experimental constraints on the conditions of formation of highly calcic plagioclase microlites at the Soufrire Hills Volcano, Montserrat. *Journal of Petrology* **44**,1455-1475 (2003).

26. Shea, T. & Hammer, J. E. Kinetics of cooling-and decompression-induced crystallization in hydrous mafic-intermediate magmas. *Journal of Volcanology and Geothermal research* **260**, 127-145 (2013).

27. Agostini, C., Fortunati, A., Arzilli, F., Landi, P. & Carroll, M. R. Kinetics of crystal evolution as a probe to magmatism at Stromboli (Aeolian Archipelago, Italy). *Geochimica et cosmochimica acta* **110**, 135-151 (2013).

28. Vona, A. & Romano, C. The effects of undercooling and deformation rates on the crystallization kinetics of Stromboli and Etna basalts. *Contributions to Mineralogy and Petrology* **166**, 491-509 (2013).

29. Kolzenburg, S., Giordano, D., Hess, K. U. & Dingwell, D. B. Shear Rate-Dependent Disequilibrium Rheology and Dynamics of Basalt Solidification. *Geophysical Research Letters* **45**, 6466-6475 (2018).

30. Marsh, B. D. (1998). On the interpretation of crystal size distributions in magmatic systems. *Journal of Petrology*, *39*(4), 553-599.

31. Cashman, K. V. Relationship between plagioclase crystallization and cooling rate in basaltic melts. *Contributions to Mineralogy and Petrology* **113**, 126-142 (1993).

32. Conte, A. M., Perinelli, C. & Trigila, R. Cooling kinetics experiments on different Stromboli lavas: Effects on crystal morphologies and phases composition. *Journal of Volcanology and Geothermal Research* **155**, 179-200 (2006).

33. Szramek, L., Gardner, J. E. & Hort, M. Cooling-induced crystallization of microlite crystals in two basaltic pumice clasts. *American Mineralogist* **95**, 503-509 (2010).

34. Brugger, C. R. & Hammer, J. E. Crystallization kinetics in continuous decompression experiments: implications for interpreting natural magma ascent processes. *Journal of Petrology* **51**, 1941-1965 (2010).

35. Karagadde, S., Lee, P. D., Cai, B., Fife, J. L., Azeem, M. A., Kareh, K. M., Puncreobutr, C., Tsivoulas, D., Connolley, T. & Atwood, R. C. Transgranular liquation cracking of grains in the semi-solid state. *Nature communications* **6**, 8300 (2015).

36. Polacci, M., Arzilli, F., La Spina, G., Le Gall, N., Cai, B., Hartley, M. E., Di Genova, D., Vo, N. T., Nonni, S., Atwood, R. C., Llewellin, E. W., Lee, P. D. & Burton, M. R. Crystallisation in basaltic magmas revealed via in situ 4D synchrotron X-ray microtomography. *Scientific Reports* **8**, 8377 (2018).

37. Goepfert, K. & Gardner, J. E. Influence of pre-eruptive storage conditions and volatile contents on explosive Plinian style eruptions of basic magma. *Bulletin of Volcanology* **72**, 511-521 (2010).

533 38. Szramek, L. A. Mafic Plinian eruptions: Is fast ascent required? *Journal of Geophysical*
534 *Research: Solid Earth* **121**, 7119-7136 (2016).
535 39. Suzuki, Y. & Fujii, T. Effect of syneruptive decompression path on shifting intensity in
536 basaltic sub-Plinian eruption: Implication of microlites in Yufune-2 scoria from Fuji volcano, Japan.
537 *Journal of Volcanology and Geothermal Research*, **198**, 158-176 (2010).
538 40. Campagnola, S., Romano, C., Mastin, L. G. & Vona, A. Confort 15 model of conduit
539 dynamics: applications to Pantelleria Green Tuff and Etna 122 BC eruptions. *Contributions to*
540 *Mineralogy and Petrology* **171**, 60 (2016).
541 41. Cassidy, M., Manga, M., Cashman, K., & Bachmann, O. (2018). Controls on explosive-
542 effusive volcanic eruption styles. Nature communications, 9, 2839.
543 42. Namiki, A. & Manga, M. Transition between fragmentation and permeable outgassing of low
544 viscosity magmas. *Journal of Volcanology and Geothermal Research* **169**, 48-60 (2008).
545
546
547 43. Corsaro, R. A., Miraglia, L. & Pompilio, M. Petrologic evidence of a complex plumbing
548 system feeding the July-August 2001 eruption of Mt. Etna, Sicily, Italy. *B. Volcanol.* **69**, 401–421
549 (2007).
550 44. Drakopoulos, M., Connolley, T., Reinhard, C., Atwood, R., Magdysyuk, O., Vo, N., Hart,
551 M., Connor, L., Humphreys, B., Howell, G. & Davies, S. I12: the joint engineering, environment
552 and processing (JEEP) beamline at diamond light source. *Journal of synchrotron radiation* **22**, 828-
553 838 (2015).
554 45. Azeem, M. A., Lee, P. D., Phillion, A. B., Karagadde, S., Rockett, P., Atwood, R. C.,
555 Courtois, L., Rahman, K. M. & Dye, D. Revealing dendritic pattern formation in Ni, Fe and Co
556 alloys using synchrotron tomography. *Acta Materialia* **128**, 241-248 (2017).
557 46. Cloetens, P., Barrett, R., Baruchel, J., Guigay, J. P. & Schlenker, M. Phase objects in syn-
558 chrotron radiation hard X-ray imaging. *J. Phys. D. Appl. Phys.* **29**, 133–46 (1996).

559 47. O'sullivan, J. D. A fast sinc function gridding algorithm for Fourier inversion in computer
560 tomography. *IEEE transactions on medical imaging* **4**, 200-207 (1985).
561 48. Gürsoy, D., De Carlo, F., Xiao, X. & Jacobsen, C. TomoPy: a framework for the analysis of
562 synchrotron tomographic data. *Journal of synchrotron radiation* **21**, 1188-1193 (2014).
563 49. Vo, N. T., Drakopoulos, M., Atwood, R. C. & Reinhard, C. Reliable method for calculating
564 the center of rotation in parallel-beam tomography. *Opt. Express* **22**, 19078–19086 (2014).
565 50. Vo, N. T., Atwood, R. C. and Drakopoulos, M. Superior techniques for eliminating ring
566 artifacts in X-ray micro-tomography. *Optics express* **26**, 28396-28412 (2018).
567 51. Titarenko, S., Withers, P. J. & Yagola, A. An analytical formula for ring artefact suppression
568 in X-ray tomography. *Applied Mathematics Letters* **23**, 1489-1495 (2010).
569 52. Abramoff M. D., Magalhaes P. J., Ram S. J. Image processing with ImageJ. *Biophot. Int.* **11**,
570 36–42 (2004).
571 53. Arzilli, F., Mancini, L., Voltolini, M., Cicconi, M. R., Mohammadi, S., Giuli, G., Mainprice,
572 D., Paris, E., Barou, F. & Carroll, M. R. Near-liquidus growth of feldspar spherulites in trachytic
573 melts: 3D morphologies and implications in crystallization mechanisms. *Lithos* **216**, 93-105 (2015).
574 54. Arzilli, F., Polacci, M., Landi, P., Giordano, D., Baker, D. R. & Mancini, L. A novel protocol
575 for resolving feldspar crystals in synchrotron X-ray microtomographic images of crystallized
576 natural magmas and synthetic analogs. *American Mineralogist* **101**, 2301-2311 (2016).
577 55. Brun, F., Mancini, L., Kasae, P., Favretto, S., Dreossi, D. & Tromba, G. Pore3D: a software
578 library for quantitative analysis of porous media. *Nucl. Instrum. Meth. A* **615**, 326–332 (2010).
579 56. Ohser, J. & Mücklich, F. Statistical analysis of microstructure in material science. Barnett V,
580 editor. Statistics in Practice, West Sussex, England: John Wiley & Sons; (2000).
581 57. La Spina, G., Polacci, M., Burton, M. & de' Michieli Vitturi, M. Numerical investigation of
582 permeability models for low viscosity magmas: application to the 2007 Stromboli effusive eruption
583 Earth and Planetary Science Letters **473**, 279-290 (2017).

584 58. de' Michieli Vitturi, M., Clarke, A. B., Neri, A. & Voight, B. Transient effects of magma
585 ascent dynamics along a geometrically variable dome-feeding conduit. *Earth Planet. Sci. Lett.* **295**,
586 541–553 (2010).
587 59. Caricchi, L., Burlini, L., Ulmer, P., Gerya, T., Vassalli, M. & Papale, P. Non-Newtonian
588 rheology of crystal-bearing magmas and implications for magma ascent dynamics. *Earth Planet.*
589 *Sci. Lett.* **264**, 402–419 (2007).
590 60. Giordano, D., Russell, J. K. & Dingwell, D. B. Viscosity of magmatic liquids: a model. *Earth*
591 *Planet. Sci. Lett.* **271**, 123-134 (2008).
592 61. Del Carlo, P. & Pompilio, M. The relationship between volatile content and the eruptive style
593 of basaltic magma: the Etna case. *Annals of Geophysics*, **47** (2004).
594 62. Costa, A., Caricchi, L. & Bagdassarov, N. A model for the rheology of particle-bearing
595 suspensions and partially molten rocks. *Geochem. Geophys. Geosyst.* **10**, (2009).
596 63. Vona, A., Romano, C., Dingwell, D. & Giordano, D. The rheology of crystal-bearing basaltic
597 magmas from Stromboli and Etna. *Geochim. Cosmochim. Acta* **75**, 3214–3236 (2011).
598 64. Smith, P. M. & Asimow, P. D. Adiabat_1ph: a new public front-end to the MELTS,
599 pMELTS, and pHMELTS models. *Geochem. Geophys. Geosyst.* **6**, (2005).
600 65. Ghiorso, M. S. & Sack, R. O. Chemical mass transfer in magmatic processes IV. A revised
601 and internally consistent thermodynamic model for the interpola-tion and extrapolation of liquid–
602 solid equilibria in magmatic systems at elevated temperatures and pressures. *Contrib. Mineral.*
603 *Petrol.* **119**, 197–212 (1995).
604 66. Adams, B. M., Ebeida, M. S., Eldred, M. S., Geraci, G., Jakeman, J. D., Maupin, K. A.,
605 Monschke, J. A., Swiler, L. P., Stephens, J. A., Vigil, D. M., Wildey, T. M., Bohnhoff, W. J.,
606 Dalbey, K. R., Eddy, J. P., Frye, J. R., Hooper, R. W., Hu, K. T., Hough, P. D., Khalil, M.,
607 Ridgway, E. M. & Rushdi, A. DAKOTA, A Multilevel Parallel Object-Oriented Framework for
608 Design Optimization, Parameter Estimation, Uncertainty Quantification, and Sensitivity Analysis
609 Version 6.6 User's Manual Tech. rep., SAND2014-4633, Tech. rep., SAND2014-4633, (2017).

Supplementary information is available in the online version of the paper.

Acknowledgements

The research leading to these results has received funding from the RCUK NERC DisEqm project (NE/N018575/1) and (NE/M013561/1). The beamtime on I12 was provided by Diamond Light Source (EE16188-1) and laboratory space by the Research Complex at Harwell.

Author Contributions

M.P., F.A., M.R.B., and P.D.L. conceived the research project. F.A., M.P., G.L.S., N.L.G., B.C., M.E.H., D.D.G., N.T.V., S.N., R.C.A., E.W.L., P.D.L. and M.R.B. contributed to the beamline experiments. F.A. collected the volcanic rocks for the starting material. D.D.G., H.M and R.A.B. prepared the starting material. F.A., M.P. and G.L.S performed image reconstruction. F.A. and M.P. performed image processing. F.A. performed image segmentation and analysis. G.L.S. performed simulations using the conduit model. R.A.B. and F.A. performed ex situ decompression experiments. E.C.B., F.A. and G.L.S. collected samples of the Etna 122 BC Plinian eruption. E.C.B. and F.A. acquired and analysed back-scattered electron images of Etna Plinian eruption's samples. F.A., G.L.S., M.R.B., M.P. and E.C.B. wrote the manuscript, with contributions from all other authors.

Author Information

Reprints and permissions information is available at www.nature.com/reprints. The authors declare no competing financial interests. Readers are welcome to comment on the online version of the paper. Correspondence and requests for materials should be addressed to F.A. (fabio.arzilli@manchester.ac.uk)

FIGURES

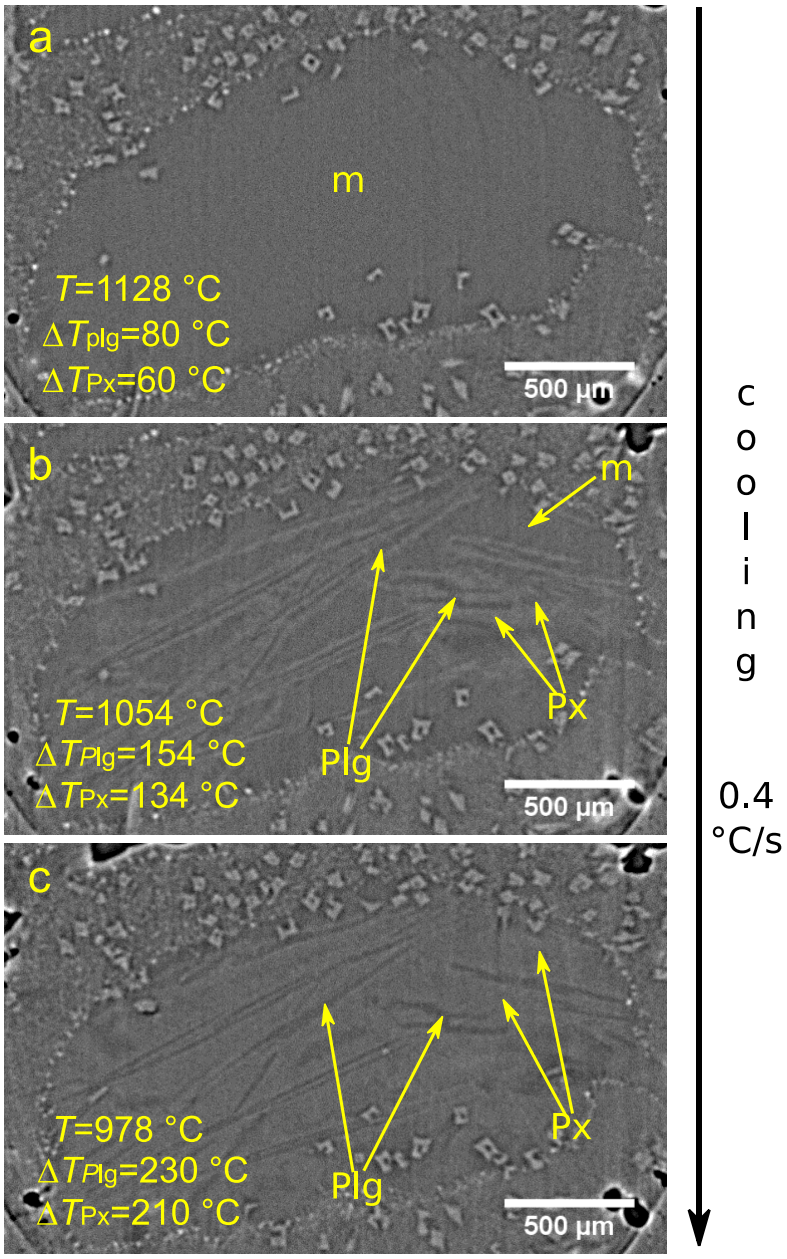

Figure 1. Crystallisation through time. Reconstructed axial slices during continuous cooling at 0.4 °Cs^{-1}: (a) frame after 24 s from the onset of the cooling, in which the temperature ranges between 1144 and 1112 °C (average 1128 °C); (b) frame after 208 s, in which the temperature ranges between 1073 and 1034 °C (average 1054 °C); (c) frame after 392 s, in which the temperature ranges between 997 and 959 °C (average 978 °C). m = melt; plg = plagioclase; px = pyroxene.

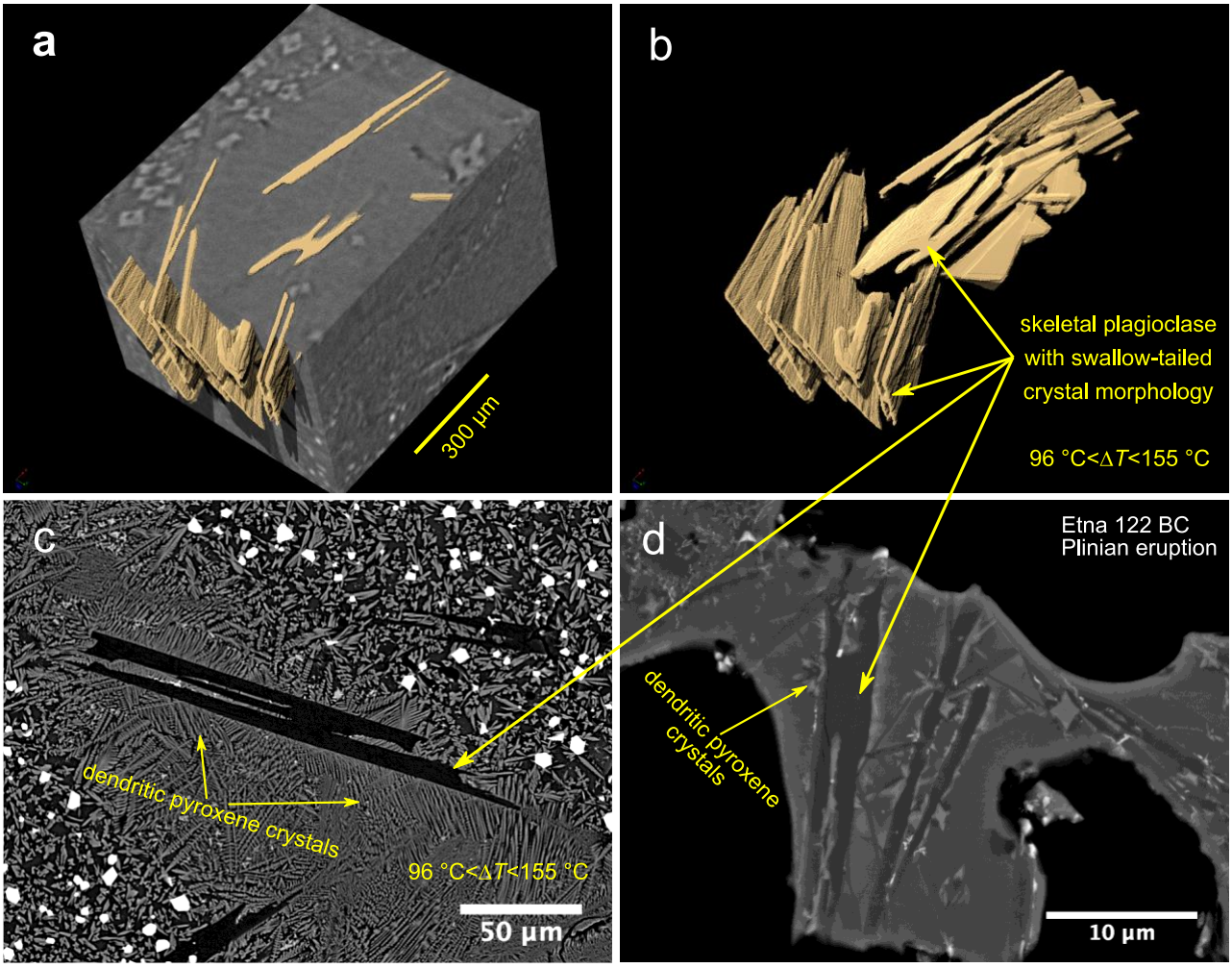

Figure 2. Plagioclase crystal morphology. (a) The 3D volume rendering of sample SS1150 shows the morphology and the spatial distribution of plagioclase crystals that formed during the rapid cooling at 96<ΔT<155 °C. (b) 3D view of the plagioclase with swallow-tailed crystal morphology. (c) Back scattered electron image of plagioclase with swallow-tailed crystal morphology. (d) Back scattered electron image of plagioclase with swallow-tailed crystal morphology produced during the Etna 122 B.C Plinian eruption. Note heterogeneous nucleation of pyroxene around plagioclase, seen as a light-coloured halo, and similar to that seen in figure 1b.

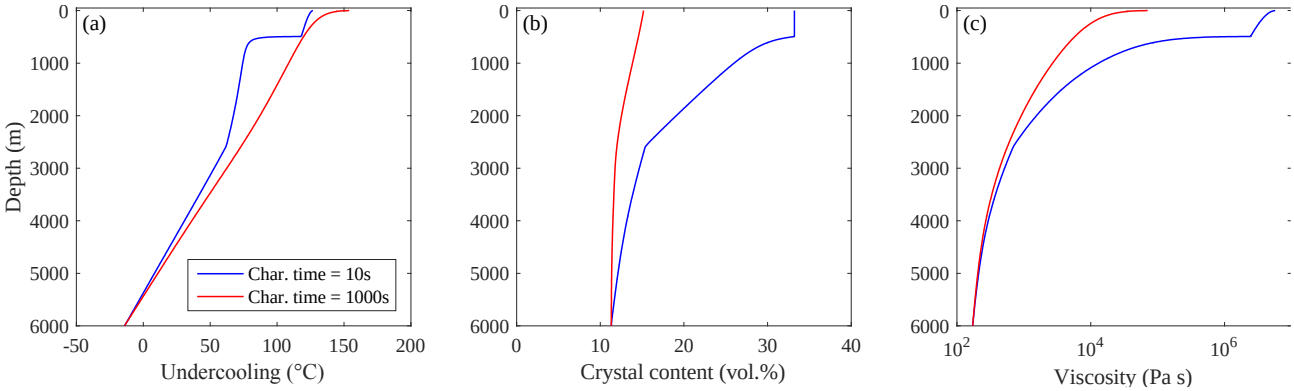

656

657

658 Figure 3. Model results during magma ascent. (a) Undercooling as a function of depth, calculated
659 for τ(c) = 10 (blue) and 1000 s (red). Cooling is driven by adiabatic expansion of gas, mitigated by
660 latent heat of crystallisation particularly in the fast crystallising case. (b) Crystal content in vol%,
661 demonstrating the rapid increase in crystal load when τ(c) = 10 s. (c) Magma viscosity,
662 demonstrating that the higher crystal load produces 3-4 order of magnitude increase in viscosity,
663 leading to fragmentation.

664

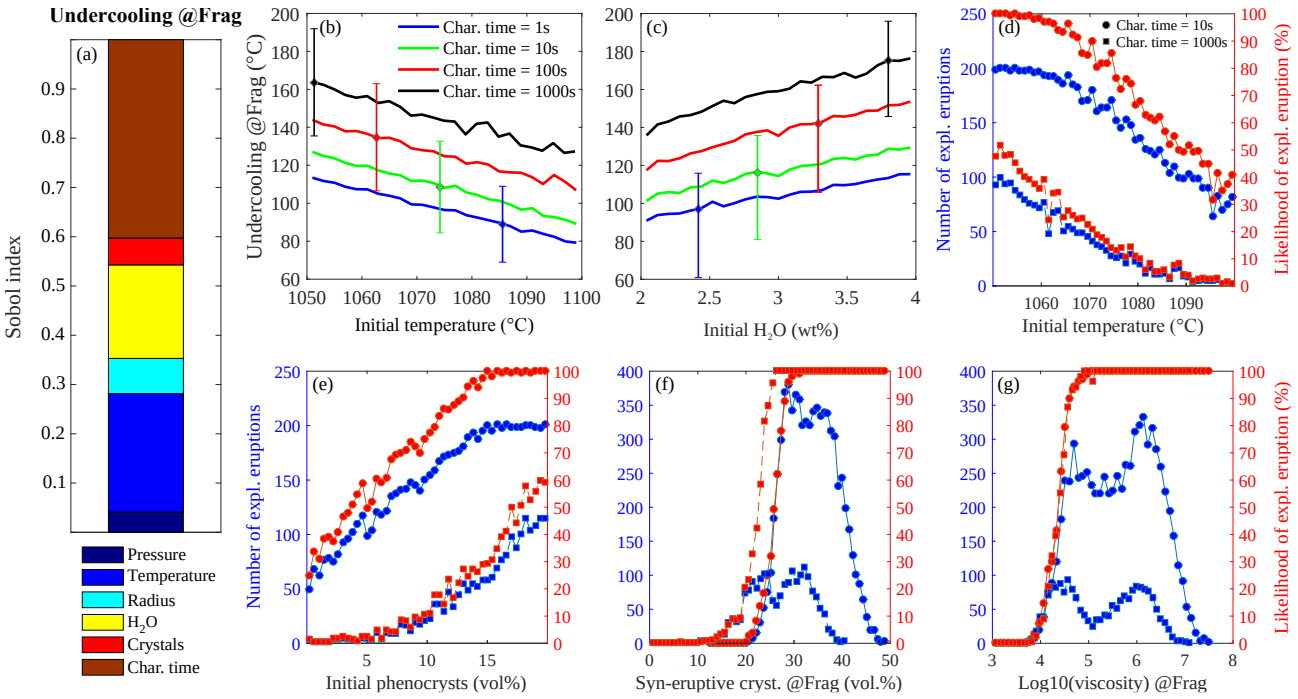

Figure 4. Relationships between characteristic time, initial temperature, initial H_2O content of the magma, syn-eruptive crystal content and magma viscosity and the undercooling of the system at the fragmentation level. These figures were calculated using repeated runs of the model while changing individual parameters to reveal the sensitivity of the system to each parameter. Likelihood of explosive eruption as a function of a specific parameter arises from the ratio between the number of model runs producing explosive eruptions divided by the total number of model runs used to test that parameter. Therefore, this is not a probabilistic assessment of eruption risk, but instead depends on the critical model parameters, which control when fragmentation occurs, and the calculated probabilities depend on the choice of upper and lower limits chosen for each investigated parameter. (a) Sobol index. (b) Undercooling vs magma temperature before ascent. (c) Undercooling vs the initial H_2O content of the magma (dissolved and exsolved). For a given input value, the solid lines are the mean of a given output parameter obtained from all the simulations assuming that input value. The error bars, instead, represent the spread of that output values with respect to the corresponding mean. (d) Frequency of explosive eruptions vs magma temperature before ascent. (e) Explosion frequency vs initial phenocryst content. (f) Frequency of explosive

682 eruptions vs syn-eruptive crystal content at the fragmentation level. (g) Frequency of explosive
683 eruptions vs magma viscosity at the fragmentation level.
684

Supplementary Information

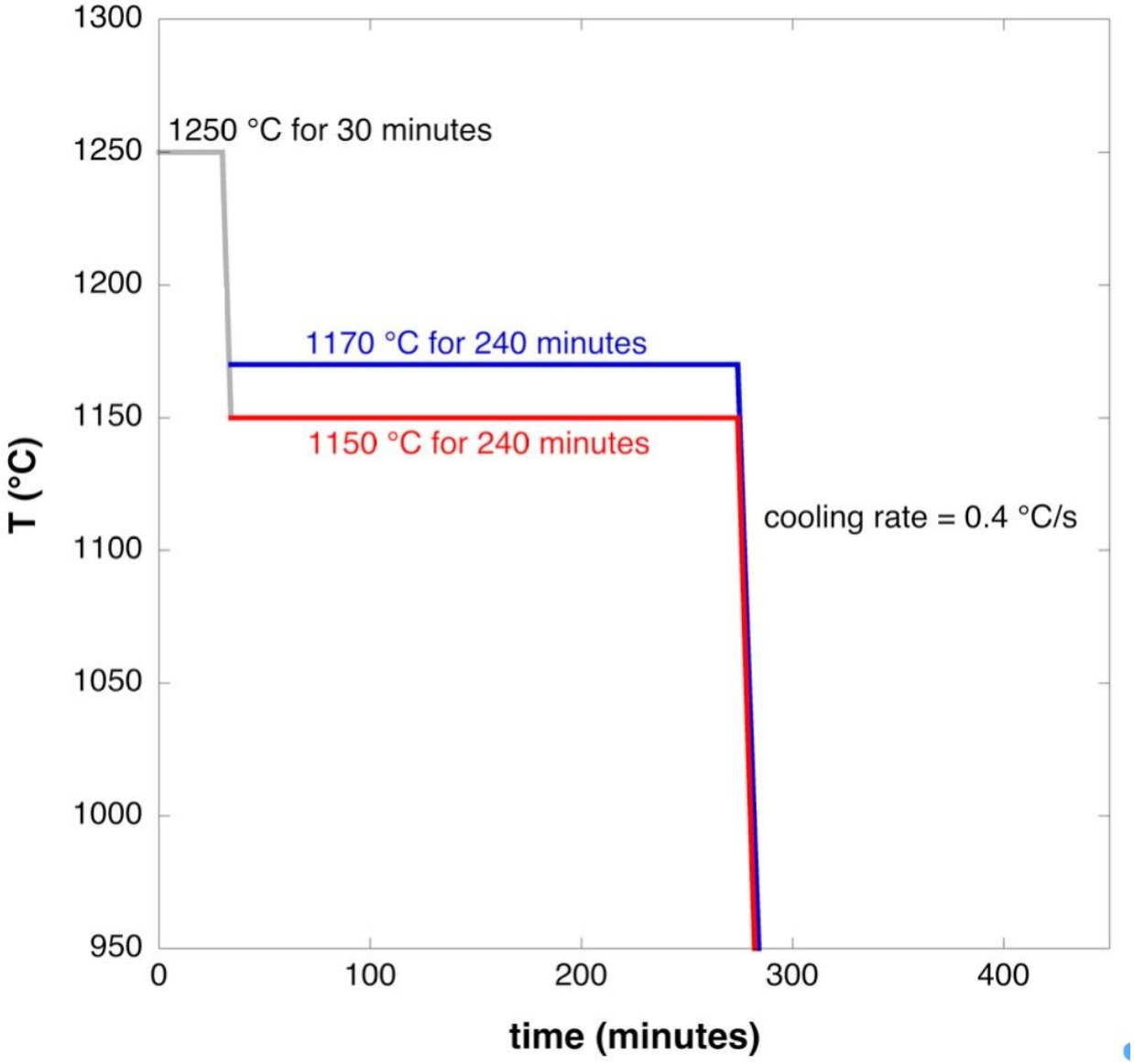

Supplementary Figure 1. Experimental conditions of *in situ* 4D experiments. The glassy cylinders were heated in situ in the Alice furnace up to 1250 ℃ for 30 minutes. After the initial annealing period, crystallisation was induced by decreasing temperature from 1250 ℃ to 1170 ℃ (SS1170) or 1150 ℃ (SS1150) at ambient pressure, holding at the final temperature for 240 minutes. After this step, the temperature was perturbed by a rapid cooling at rate of 0.4 ℃/s, reaching ~950 ℃ in ~8 minutes.

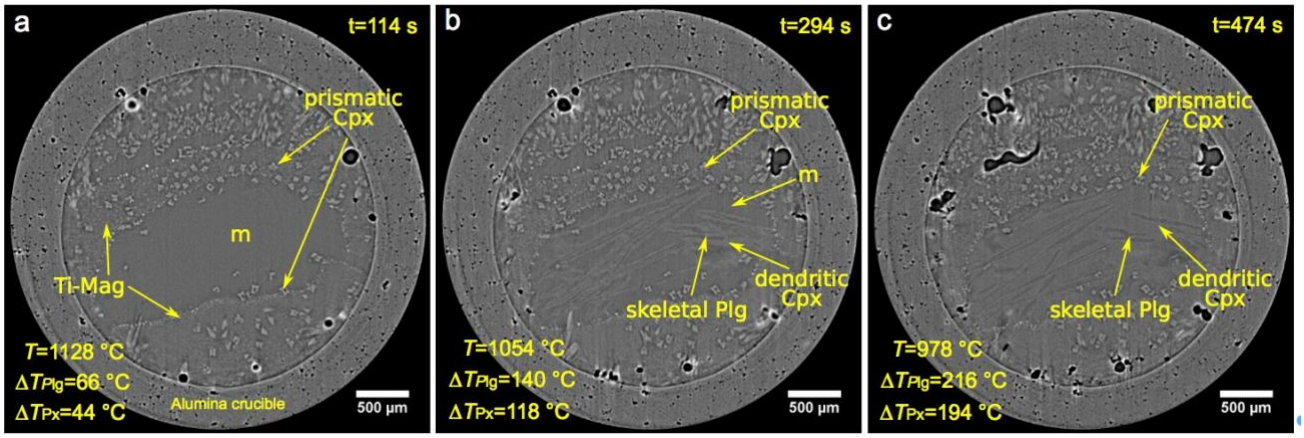

Supplementary Figure 2. Crystallisation through time during experiment SS1150. Reconstructed axial slices during continuous cooling at 0.4 °C s^{-1}: **a,** frame represents the texture after 114 s from the onset of the cooling in which the temperature ranges between 1144 and 1112 °C (average 1128 °C); **b,** frame after 294 s, in which the temperature ranges between 1073 and 1034 °C (average 1054 °C); **c,** frame after 474 s, in which the temperature ranges between 997 and 959 °C (average 978 °C). m = melt; Plg = plagioclase; Cpx = clinopyroxene; Ti-Mag: titanomagnetite. The acquisition time of each frame is 90 s. t = time from the onset of the cooling to the end of the frame acquisition.

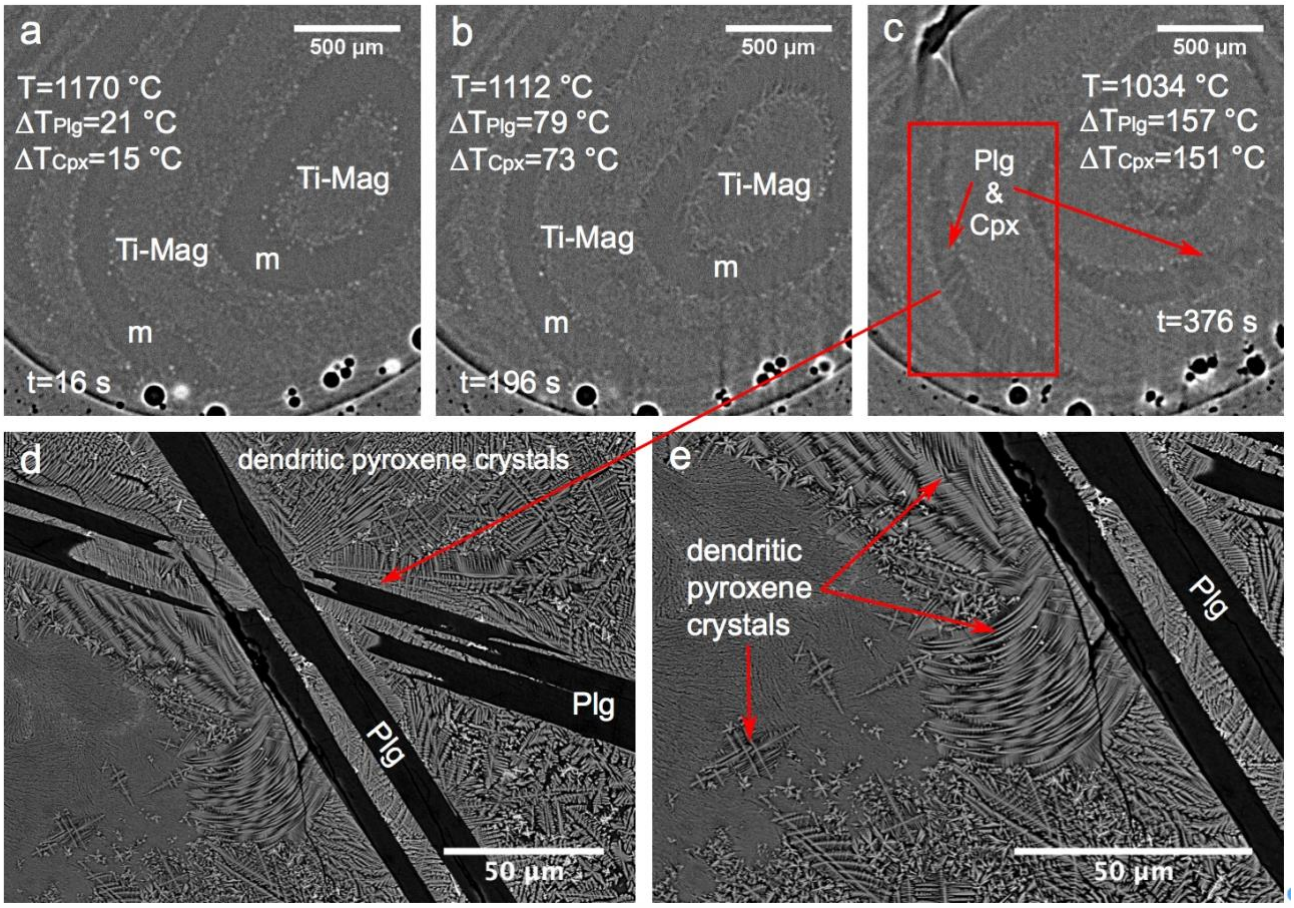

Supplementary Figure 3. Crystallisation through time during experiment SS1170. Reconstructed axial slices during continuous cooling at 0.4 °C s^{-1}: **a,** this frame shows the first 16 s from the onset of the cooling, in which the temperature ranges between 1170 and 1165 °C; **b,** frame after 196 s, in which the temperature ranges between 1131 and 1092 °C (average 1112 °C); **c,** frame after 376 s, in which the temperature ranges between 1053 and 1015 °C (average 1034 °C). m = melt; Plg = plagioclase; Cpx = pyroxene; Ti-Mag: titanomagnetite. The acquisition time of each frame is 90 s. t = time from the onset of the cooling to the end of the frame acquisition.

733 -

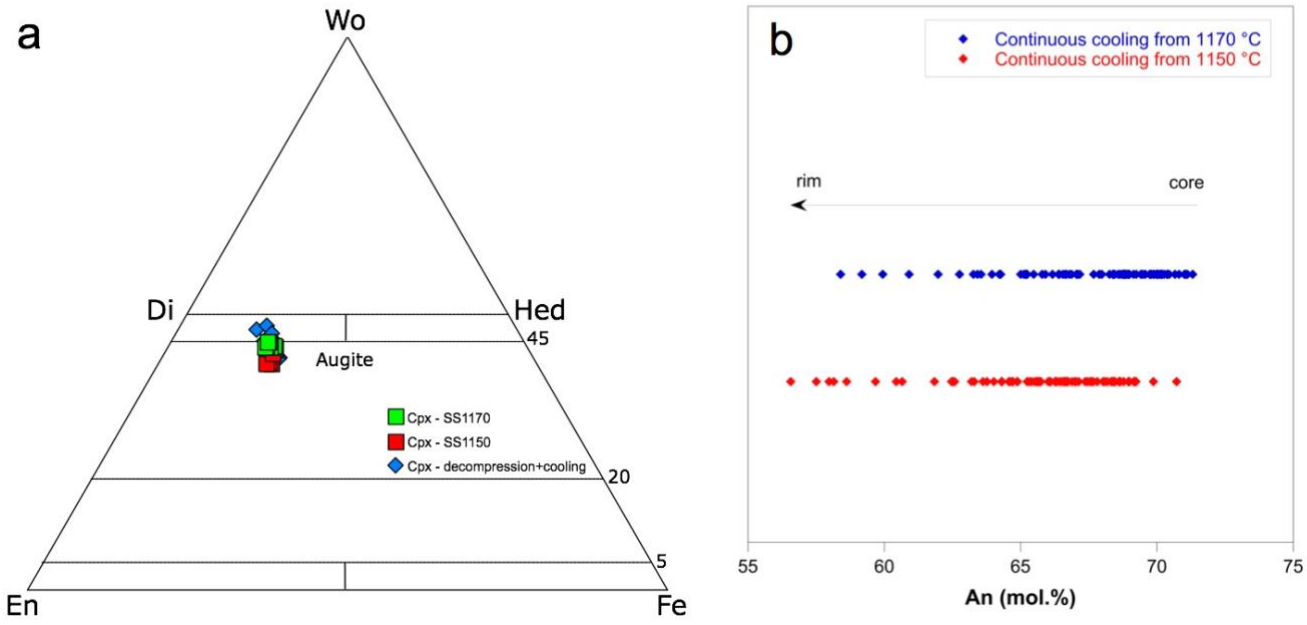

734

735 **Supplemetary Figure 4. Chemical compositions of pyroxene and plagioclase formed during**
736 **experiments. a,** Compositions of pyroxene crystals during rapid cooling at ambient pressure
737 (SS1170 and SS1150) and rapid decompressionand cooling (Etna_7_C): green square=SS1170; red
738 square=SS1150; blue diamond=Etna_7_C. En: enstatite; Fs: ferrosilite; Di: diopside; Hd:
739 hedenbergite; Wo: Wollastonite. **b,** Anorthite contents of plagioclase crystals formed during *in situ*
740 experiments (SS1170 and SS1150).

741
742
743
744
745

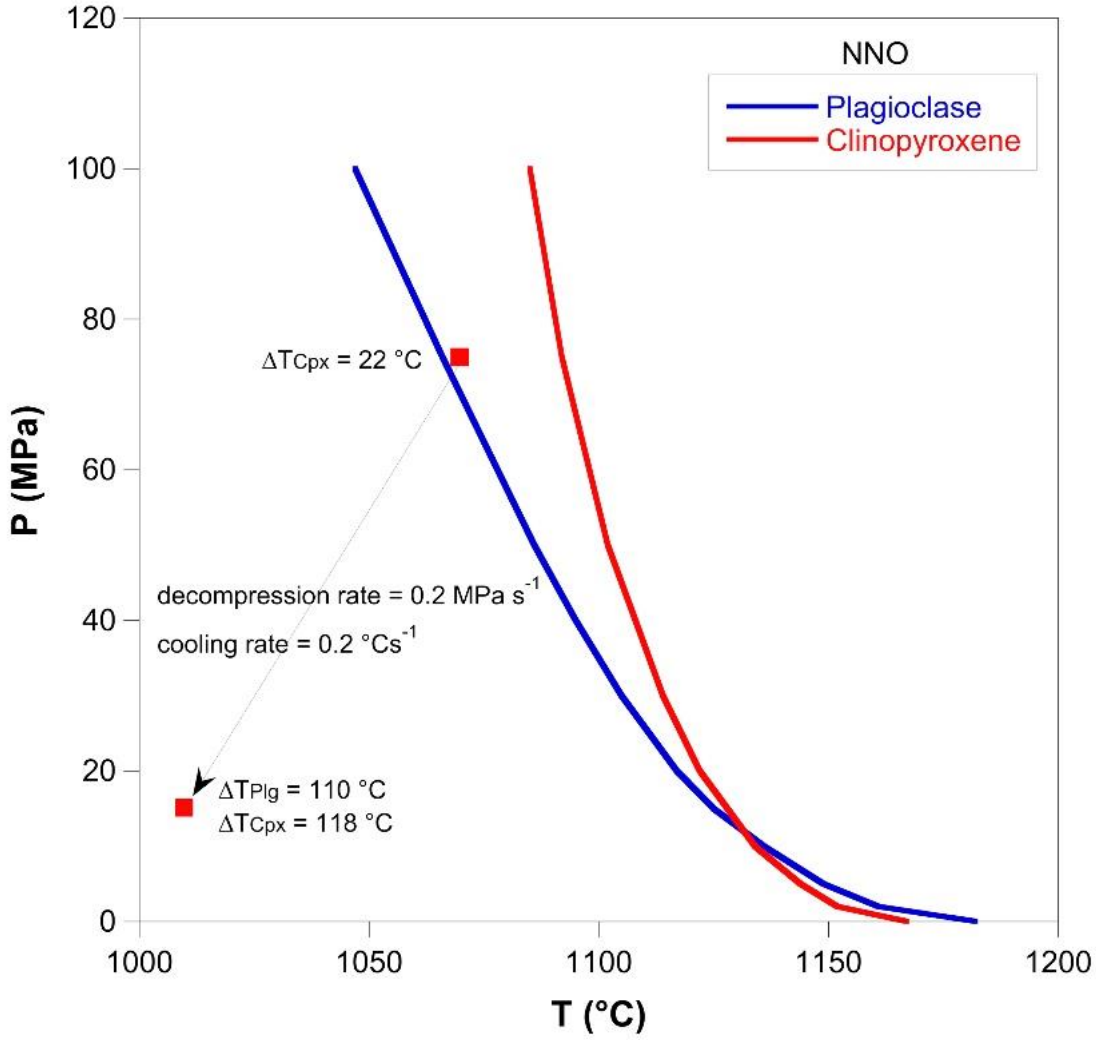

Supplementary Figure 5. *Ex situ* experimental conditions of rapid cooling and decompression experiment. The experimental approach consisted of holding the sample for 30 minutes at 75 MPa and 1070 °C before being decompressed and cooled. The first experiment was quenched after 30 minutes at 75 MPa and 1070 °C, in order to texturally characterise the initial conditions before that fast decompression and cooling were applied. In the second experiment, after 30 minutes pressure and temperature were decreased continuously in 300 s at 0.2 MPa s^{-1} and 0.2 °Cs^{-1} respectively, reaching 15 MPa and 1010 °C Final pressure was chosen as approximate fragmentation pressures calculated by modeling. Decompression and cooling rates were predicted from the conduit model used in this study. Plagioclase and clinopyroxene liquidi were obtained with Rhyolite-MELTS software (version 1.2), using the composition of our starting material.

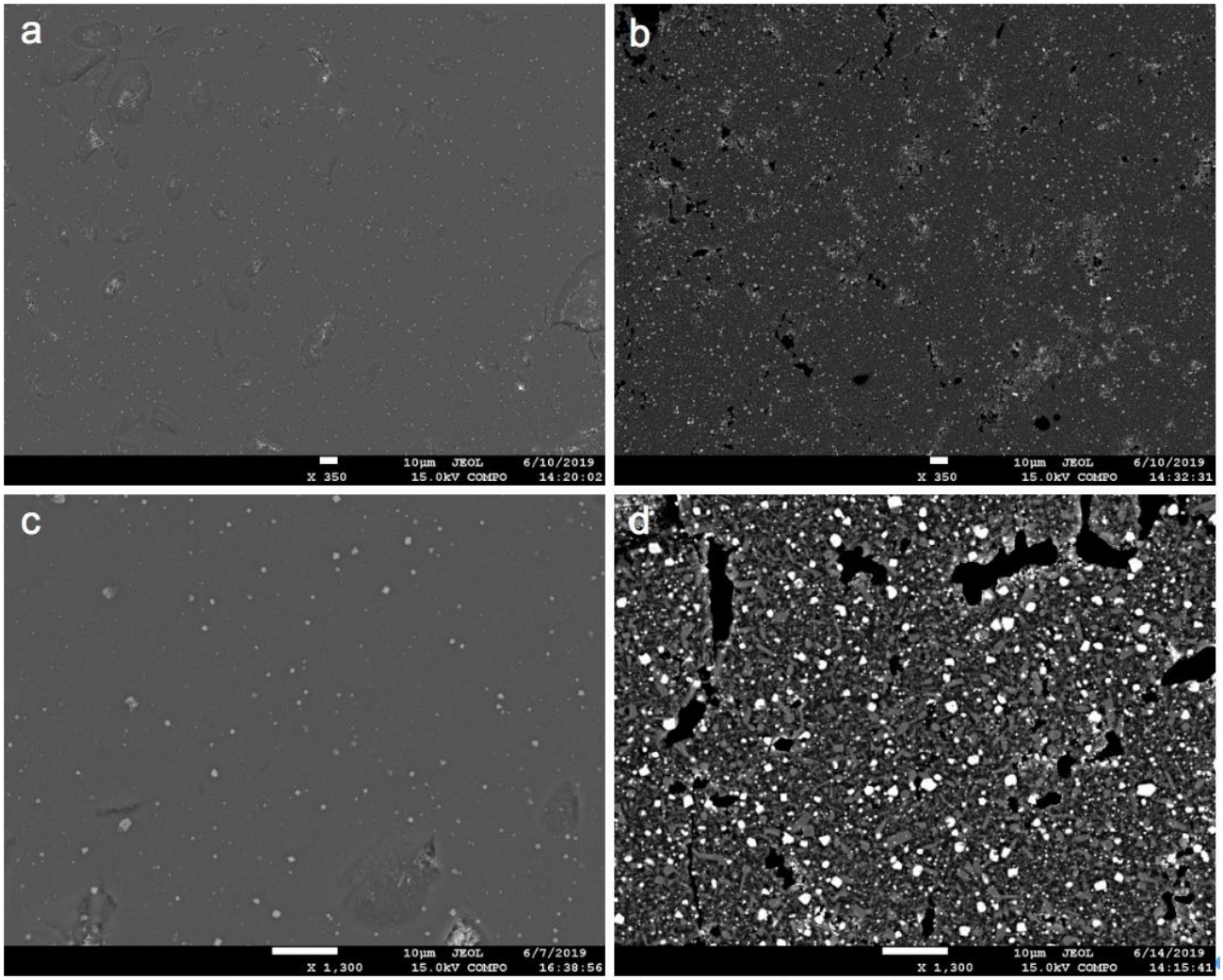

Supplementary Figure 6. Textures of *ex situ* experiments. Back scattered images show the textures of: **a**, **c**, an hydrous basalt quenched at 75 Mpa and 1070 °C after 30 minutes (sample Etna7_C) and **b**, **d**, an hydrous basalt quenched after a rapid decompression and cooling at 15 MPa and 1010 °C (sample Etna7_B). **a**, **c**, The texture of sample Etna7_C is characterised by oxide crystals and glassy matrix. **b**, **d**, The mineral assemblage of sample Etna7_B consists of oxide, clinopyroxene and plagioclase. Oxide formed mostly at initial condtions, after 30 minutes at 1070 °C and 75 MPa (see Etna7_C, panels **a** and **c**). The rapid decompression and cooling allowed the achievement of large ΔTs (>100 °C; see Supplementary Fig. 6) in 300 s, favouring predominantly clinopyroxene crystallisation, plagioclase and oxide. This indicates that $\tau^{(c)}$ is 60 s, in agreement with the order of magnitude estimated from *in situ* experiments.

Supplementary Table 1. Chemical composition of the starting material.

Oxide (wt.%)	Bulk composition	st. dev.	Residual melt after 4h at 1170 °C	Residual melt after 4h at 1150 °C
SiO_2	48.41	0.16	52.18	52.99
TiO_2	1.79	0.07	1.7	1.69
Al_2O_3	16.22	0.50	16.86	17.5
FeO*	10.66	0.30	6.05	5.4
MnO	0.20	0.03	0.22	0.24
MgO	6.20	0.32	5.34	4.77
CaO	10.66	0.19	11.23	10.54
Na_2O	3.41	0.20	3.74	3.99
K_2O	1.90	0.07	2.09	2.24
P_2O_5	0.54	0.04	0.59	0.64
Total	99.85		100	100

note: FeO* = total iron as FeO. The residual melt compositions after the 240 minutes have been obtained with a mass balance calculation, which indicates that they are basaltic trachyandesite. We considered that the main difference between experiment SS1150 and SS1170 is that the abundance of pyroxene after 4 hours at 1150 °C is higher than that at 1170 °C. Experiment SS1170 (after 4 hour at 1170 °C) indicates that prismatic pyroxene crystals are ~ 1 vol.% and oxide crystals are ~8 vol. %, whereas in the experiment SS1150 (after 4 hour at 1150 °C) prismatic pyroxene crystals are more abundant (~8 vol.%).

Supplementary Table 2. Results of plagioclase and pyroxene growth rates during continuous cooling at 0.4 °C/s.

3D analysis

Plagioclase crystal growth rate

Sample	Growth duration (s)	L3Dmax (cm)	YL3Dmax (cm s^{-1})	L3Dmin (cm)	YL3Dmin (cm s^{-1})	L3Dave (cm)	YL3Dave (cm s^{-1})
SS1150	90	2.77E-02	1.54E-04	6.35E-03	3.53E-05	1.39E-02	7.74E-05

2D analysis

Plagioclase crystal growth rate

Sample	Growth duration (s)	Lmax (cm)	YLmax (cm s^{-1})	Lmin (cm)	YLmin (cm s^{-1})	Lave (cm)	YLave (cm s^{-1})
SS1170	180	2.73E-02	7.59E-05	1.15E-02	3.20E-05	1.78E-02	4.96E-05

Pyroxene crystal growth rate

Sample	Growth duration (s)	Lmax (cm)	YLmax (cm s^{-1})
SS1170	180	3.6E-03	2.0E-05
SS1150	180	3.24E-03	1.80E-05

note: L3Dmax = average length of the 15 largest crystals measured in the 3D domain; YL3Dmax = growth rate calculated using the 15 largest crystals; L3Dmin = average length of the 15 smallest crystals measured in the 3D domain; YL3Dmin = growth rate calculated using the 15 smallest crystals; YL3Dave = the average value of growth rate obtained taking into account the length all the crystals analysed; Lmax = average length of the 15 largest crystals measured in the 2D domain; YLmax = growth rate calculated using the 15 largest crystals.

Supplementary Table 3. Experimental conditions for ex situ experiments performed with TZM cold seal pressure vessel apparatus.

Sample	Ti (°C)	Pi (Mpa)	ti (s)	decompression rate (Mpa s-1)	cooling rate (°Cs-1)	Tf	Pf
Etna7_C	1070	75	1800	-	-	1070	75
Etna7_B	1070	75	1800	0.2	0.2	1010	15

Supplementary Table 4. Summary of X-ray microtomography acquisition conditions and image processing details of the volumes of interest (VOI) for experiment ET1150.

Energy	Distance sample to detector	Projection	Exposure time	Voxel size	Original imaged volume	Analysed VOI	Segmentation
keV	mm	number	s	μm^3	pixels (mm^3)	mm^3	
53	2300	1800	0.05	3.2x3.2x3.2	1683x1683x1383 (128.4)	8.2037	semi-automatic volume segmentation Avizo software v. 8.0